Cone-beam reconstruction for the two-circles-plus-one-line trajectory

2012 Phys. Med. Biol. 57 2689

(http://iopscience.iop.org/0031-9155/57/9/2689)

IOP PUBLISHING PHYSICS IN MEDICINE AND BIOLOGY

Phys. Med. Biol. **57** (2012) 2689–2707 doi:10.1088/0031-9155/57/9/2689

Cone-beam reconstruction for the two-circles-plus-one-line trajectory

Yanbin Lu[1], Jiansheng Yang[1], John W Emerson[2], Heng Mao[1], Tie Zhou[1], Yuanzheng Si[1] and Ming Jiang[1]

[1] LMAM, School of Mathematical Sciences, Peking University, Beijing, 100871, People's Republic of China

[2] Department of Statistics, Yale University, New Haven, CT 06511, USA

E-mail: luyanbin@pku.edu.cn, jsyang@pku.edu.cn, john.emerson@yale.edu, heng.mao@pku.edu.cn, tie.zhou@pku.edu.cn, yuanzhengsi@gmail.com and ming-jiang@ieee.org

Received 13 July 2011, in final form 10 March 2012

Published 17 April 2012

Online at stacks.iop.org/PMB/57/2689

Abstract

The Kodak Image Station *In-Vivo* FX has an x-ray module with cone-beam configuration for radiographic imaging but lacks the functionality of tomography. To introduce x-ray tomography into the system, we choose the two-circles-plus-one-line trajectory by mounting one translation motor and one rotation motor. We establish a reconstruction algorithm by applying the M-line reconstruction method. Numerical studies and preliminary physical phantom experiment demonstrate the feasibility of the proposed design and reconstruction algorithm.

(Some figures may appear in colour only in the online journal)

1. Introduction

X-ray computed tomography (XCT) plays an instrumental role in emerging optical molecular imaging techniques in addition to other structural imaging modalities such as magnetic resonance imaging (MRI) (Ntziachristos *et al* 2005, Arridge and Schotland 2009). In bioluminescence tomography, XCT image volumes are segmented to generate the geometrical modelling of underlying objects and then optical property mapping is introduced to provide the optical properties of anatomical structures for the bioluminescent source reconstruction (Wang *et al* 2004, Jiang *et al* 2007, Gu *et al* 2004). Because optical tomography provides only functional images with insufficient resolution, XCT or MRI is indispensible for other optical modalities such as diffuse optical tomography (Yalavarthy *et al* 2007), and florescence molecular tomography (Schulz *et al* 2010) at present. Hybrid systems that combine the advantages of multiple modalities are under active development (Wang *et al* 2006, Alexandrakis *et al* 2005, Ntziachristos *et al* 2005).

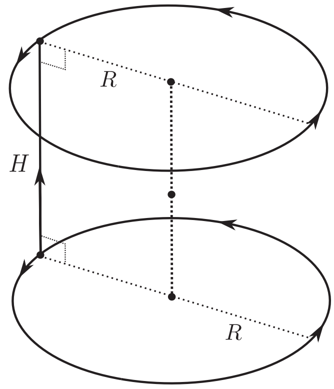

Figure 1. The two-circles-plus-one-line trajectory. The arrows indicate the directions of the source movement.

We have been working on a multi-modality imaging system for small animals in our laboratory. The system is built upon a commercial product, Kodak Image Station *In-Vivo* FX (Carestream Health, Inc., Rochester, NY) (McLaughlin and Vizard 2006). The current system has an x-ray module with cone-beam configuration for radiographic imaging but lacks the functionality of tomography. We first need to improve the x-ray module by introducing rotational and translational mechanical components to enable it for tomographic imaging. The x-ray module is contained in a cabinet room with a dimension of length ≈560 mm, width ≈350 mm and height ≈440 mm. The room provides a very limited space to work out the implementation of the add-on mechanical components. Moreover, the radiographic phosphor screen for photo converse is fixed at one side of the cabinet room, which further reduces our work space to half of the cabinet room. For exact cone-beam XCT reconstruction, we need to find an efficient imaging geometry that works in such a small space. There are various possible imaging geometries for us to choose from for exact cone-beam XCT reconstruction. After analysis and comparison of several candidate imaging geometries and corresponding exact reconstruction methods for cone-beam XCT, we found that a two-circles-plus-one-line trajectory shown in figure 1 is preferable. Please refer to the discussions for details.

Cone-beam XCT has been extensively studied in the past decades. In Defrise and Clack (1994), the authors proposed that a general cone-beam filtered-backprojection (FBP) algorithm for any trajectory satisfies Tuy's condition (Tuy 1983). Kudo and Saito reformulated the results in Smith (1985) and Tuy (1983) and proposed a cone-beam reconstruction algorithm for non-planar orbits (Kudo and Saito 1994). Katsevich reported the first exact shift-invariant FBP reconstruction formula for helical XCT using more data than the Tam–Dannielson window (Katsevich 2002). In Katsevich (2004b), this data requirement was reduced. Zou and Pan established a backprojection-filtration (BPF) format formula using data only within the Tam–Dannielson window (Zou and Pan 2004).

Helical cone-beam XCT (also called spiral cone-beam XCT) and its generalization to arbitrary source trajectory exhibited flourishing development in the last decade. Katsevich developed a general cone-beam FBP formula based on the Grangeat formula (Grangeat 1991) using a general weight function (Katsevich 2003). Chen proposed an alternative derivation of the Katsevich formula based on the Tuy formula (Tuy 1983) with relaxed Tuy's data sufficiency condition (Chen 2003). Pack *et al* proved a BPF reconstruction formula for both a single curve and multiple smooth curves (Pack *et al* 2005). In their work, redundantly measured lines (R-lines) and measured lines (M-lines) in image space were introduced for exact reconstruction

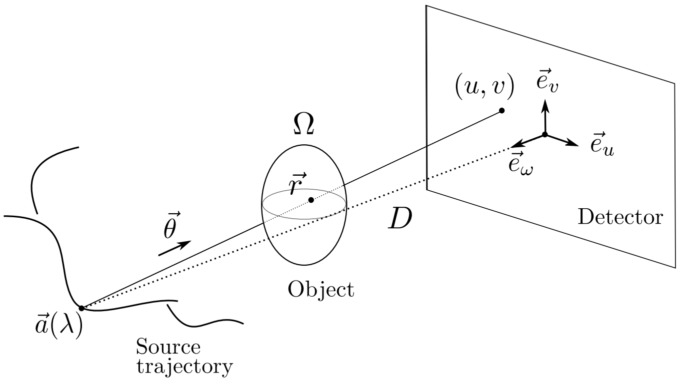

Figure 2. The cone-beam projection and the coordinate system in the detector plane.

for various source trajectories to provide the flexibility in choosing the backprojection of locally filtered projections. A measured line (M-line) is a line which contains only one source position and is part of the measurements, while a redundantly measured line (R-line) is a line segment that connects two source positions (Pack *et al* 2005). Ye *et al* proposed a generalized BPF formula for reconstruction on R-lines for a single smoothing source trajectory in Ye *et al* (2005). Ye and Wang established a FBP formula and gave suggestions for filtering directions for a smooth curve (Ye and Wang 2005). In Zhao *et al* (2005), the authors provided a new proof for Katsevich's formula and extended Zou and Pan's formula to any interior point on an R-line on a continuous source trajectory. Pack and Noo demonstrated a FBP reconstruction formula using 1D filtering along the projection of M-lines for multiple source curves (Pack and Noo 2005). R-lines are also alternatively called chords in Zhao *et al* (2005), Ye *et al* (2005) and Ye and Wang (2005).

In this paper, we are to develop a BPF algorithm for the two-circles-plus-one-line trajectory for our imaging application based on the result in Pack *et al* (2005). This two-circles-plus-one-line trajectory consists of two circles with the same radius R in two parallel planes, respectively, and one line segment with length H perpendicular to the two planes as shown in figure 1. The two circles are oriented counterclockwise. In Yu *et al* (2011), the R-line coverage of the arc–line–arc trajectory has been studied intensively. It has been proved that the R-lines for the two-circles-plus-one-line trajectory can fully cover the region inside this trajectory. Hence, the two-circles-plus-one-line trajectory satisfies the conditions for exact XCT reconstruction in Pack *et al* (2005). Therefore, by the general reconstruction algorithm in Pack *et al* (2005), the exact reconstruction on an M-line covered by R-lines inside the trajectory can be achieved.

The paper is organized as follows. In section 2, we apply the M-line reconstruction formula for the two-circles-plus-one-line trajectory, and analyse the geometric properties of R-lines. In section 3, we report numerical studies and a preliminary physical phantom experiment for the reconstruction formula. In section 4, we discuss relevant issues. We conclude the paper in section 5.

2. Method

2.1. Notations

We use similar notations as in Pack *et al* (2005). Let Ω be a bounded convex neighbourhood containing an object in R^3. The source trajectory $\vec{a}$, which is described by the parameter λ,

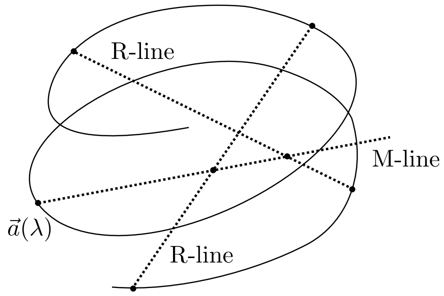

Figure 3. M-lines and R-lines (dotted lines in this figure).

consists of N smooth curves Γ_j, $j = 1, \ldots, N$, such that a neighbourhood of each curve lies outside Ω (see figure 2). The domain of λ is a union of disjoint intervals Λ_j, $j = 1, \ldots, N$, each of which corresponds to one of the curves Γ_j, $j = 1, \ldots, N$. The tangent vector $\vec{a}'(\lambda)$ is assumed to be bounded, continuous and nonzero in the interior of each Λ_j, $j = 1, \ldots, N$. For $\vec{r} \in R^3$, let $f(\vec{r}): R^3 \to R$ be the absorption coefficient of x-ray of the object under imaging. The support of f is contained in Ω.

The cone-beam projection at the source position $\vec{a}(\lambda)$ is defined as (Natterer and Wübbeling 2001)

$$g(\lambda, \vec{\theta}) = \int_0^\infty f(\vec{a}(\lambda) + t\vec{\theta})\, \mathrm{d}t, \tag{1}$$

where $\vec{\theta} \in S^2$. Each cone-beam projection data is acquired by a flat panel detector placed on the opposite side of the object relative to the source as shown in figure 2. The detector plane intercepts all lines which diverge from the source and go through the object. The unit vector $\vec{e}_w$ is perpendicular to the detector plane. Two unit vectors $\vec{e}_u$ and $\vec{e}_v$ on the detector plane are chosen to formulate a coordinate system for the detector plane. Detector elements have coordinates (u, v) with $(u, v) = (0, 0)$ at the orthogonal projection of $\vec{a}(\lambda)$ onto the detector plane. $D(\lambda)$ is the distance from $\vec{a}(\lambda)$ to the detector plane. The detector is said to be well-oriented when $\vec{e}_u$ and $\vec{e}_w$ are parallel and orthogonal to $\vec{a}'(\lambda)$, respectively (Pack *et al* 2005). The cone-beam projection $g(\lambda, \vec{\theta})$ can also be denoted as $g(\lambda, u, v)$ where

$$\vec{\theta} = \frac{1}{\sqrt{u^2 + v^2 + D(\lambda)^2}}(u\vec{e}_u + v\vec{e}_v - D(\lambda)\vec{e}_w). \tag{2}$$

2.2. M-line reconstruction method

In this subsection, we introduce an M-line reconstruction method for a continuous and piecewise smooth source trajectory from Pack *et al* (2005). As shown in figure 3, a measured line (M-line) is a line which contains only one source position and is part of the measurements, while a redundantly measured line (R-line) is a line segment that connects two source positions.

It is proved in Pack *et al* (2005) that the Hilbert transform of f on one M-line is related to the differentiated backprojection of cone-beam projection data. The differentiated backprojection $B(\vec{r}, \lambda_1, \lambda_2)$ at any $\vec{r} \in \Omega$ over any segment $[\lambda_1, \lambda_2]$ of one of the smooth curves Γ_j is

$$B(\vec{r}, \lambda_1, \lambda_2) = \int_{\lambda_1}^{\lambda_2} \frac{D(\lambda)\|\vec{a}'(\lambda)\|}{[(\vec{a}(\lambda) - \vec{r}) \cdot \vec{e}_w]^2} \frac{\partial}{\partial u} \left[\frac{D(\lambda)}{\sqrt{D(\lambda)^2 + u^2 + v^2}} g(\lambda, u, v) \right] \Bigg|_{\substack{u=\tilde{u}(\lambda,\vec{r})\\ v=\tilde{v}(\lambda,\vec{r})}} \mathrm{d}\lambda, \tag{3}$$

where $\tilde{u} = \tilde{u}(\lambda, \vec{r})$ and $\tilde{v} = \tilde{v}(\lambda, \vec{r})$ are the local coordinates of the intersection point of the line connecting $\vec{r}$ and $\vec{a}(\lambda)$ with the detector plane, respectively,

$$\tilde{u}(\lambda, \vec{r}) = -D(\lambda)\frac{(\vec{r}-\vec{a}(\lambda))\cdot\vec{e}_u}{(\vec{r}-\vec{a}(\lambda))\cdot\vec{e}_w}, \qquad \tilde{v}(\lambda, \vec{r}) = -D(\lambda)\frac{(\vec{r}-\vec{a}(\lambda))\cdot\vec{e}_v}{(\vec{r}-\vec{a}(\lambda))\cdot\vec{e}_w}. \tag{4}$$

For a fixed $\vec{\alpha} \in S^2$, $\vec{s} \in R^3$, let

$$L(\vec{\alpha}, \vec{s}) = \{\vec{s} + t\vec{\alpha}:\ t \in R\} \tag{5}$$

and

$$k(t, \vec{\alpha}, \vec{s}) = f(\vec{s} + t\vec{\alpha}). \tag{6}$$

The Hilbert transform of f along the line $L(\vec{\alpha}, \vec{s})$ with respect to t is defined as follows:

$$Hf(t, \vec{\alpha}, \vec{s}) = \text{P.V.} \int_{-\infty}^{\infty} \frac{1}{\pi(t-t')} k(t', \vec{\alpha}, \vec{s})\, \mathrm{d}t' = \text{P.V.} \int_{-\infty}^{\infty} \frac{1}{\pi(t-t')} f(\vec{s} + t'\vec{\alpha})\, \mathrm{d}t', \tag{7}$$

where P.V. stands for the Cauchy principal integral value.

Let $\vec{r}(t, \vec{\alpha}, \vec{a}(\lambda)) = \vec{a}(\lambda) + t\vec{\alpha}$ be in the intersection of an M-line $L(\vec{\alpha}, \vec{a}(\lambda))$ and Ω, and

$$\vec{\omega}(\lambda, \vec{r}) = \frac{\vec{r}-\vec{a}(\lambda)}{\|\vec{r}-\vec{a}(\lambda)\|} \tag{8}$$

be the unit vector from $\vec{a}(\lambda)$ to $\vec{r}$. The relation between the Hilbert transform of f and the differential backprojection and boundary terms is established in Pack *et al* (2005):

$$\frac{1}{\pi}\bar{B}(\vec{r}, \lambda_1, \lambda_2) = Hf(t, \vec{\omega}(\lambda_2, \vec{r}), \vec{r})|_{t=0} - Hf(t, \vec{\omega}(\lambda_1, \vec{r}), \vec{r})|_{t=0}, \tag{9}$$

where

$$\bar{B}(\vec{r}, \lambda_1, \lambda_2) = B(\vec{r}, \lambda_1, \lambda_2) + \frac{g(\lambda_2, \vec{\omega}(\lambda_2, \vec{r}))}{\|\vec{r}-\vec{a}(\lambda_2)\|} - \frac{g(\lambda_1, \vec{\omega}(\lambda_1, \vec{r}))}{\|\vec{r}-\vec{a}(\lambda_1)\|}, \tag{10}$$

and $[\lambda_1, \lambda_2]$ is a segment of one of the smooth curves.

In fact, equation (9) holds for any segment of a continuous and piece-wise smooth source trajectory because such segment can be divided into several smooth parts. Therefore, the M-line reconstruction method for one single smooth curve in Pack *et al* (2005) also holds for a continuous and piece-wise smooth source trajectory, as follows:

$$Hf(t, \vec{\alpha}, \vec{a}(\lambda)) = -\frac{1}{2\pi}(\bar{B}(\vec{r}(t, \vec{\alpha}, \vec{a}(\lambda)), \lambda, \lambda') + \bar{B}(\vec{r}(t, \vec{\alpha}, \vec{a}(\lambda)), \lambda, \lambda'')), \tag{11}$$

where $\vec{a}(\lambda')$ and $\vec{a}(\lambda'')$ are the endpoints of one R-line passing through $\vec{r} \in L(\vec{\alpha}, \vec{a}(\lambda))$. Let $[t_{\min}, t_{\max}]$ be the interval such that $k(t, \vec{\alpha}, \vec{a}(\lambda)) = 0$ for $t \notin [t_{\min}, t_{\max}]$. Then f can be reconstructed by applying the finite inverse Hilbert transform to $Hf(t, \vec{\alpha}, \vec{a}(\lambda))$ (Tricomi 1951, Pack *et al* 2005). The reconstruction formula for f is as follows:

$$f(\vec{r}) = k(t, \vec{\alpha}, \vec{a}(\lambda))|_{t=(\vec{r}-\vec{a}(\lambda))\cdot\vec{\alpha}} = \frac{C(\vec{\alpha}, \vec{a}(\lambda)) - \bar{f}(t, \vec{\alpha}, \vec{a}(\lambda))}{w(t, \vec{\alpha}, \vec{a}(\lambda))} \quad \text{for } t \in [t_{\min}, t_{\max}], \tag{12}$$

where

$$w(t, \vec{\alpha}, \vec{a}(\lambda)) = \sqrt{(t-t_{\min})(t_{\max}-t)}, \tag{13}$$

$$\bar{f}(t, \vec{\alpha}, \vec{a}(\lambda)) = \int_{t_{\min}}^{t_{\max}} \frac{w(t', \vec{\alpha}, \vec{a}(\lambda))}{\pi(t-t')} Hf(t', \vec{\alpha}, \vec{a}(\lambda))\, \mathrm{d}t', \tag{14}$$

$$C(\vec{\alpha}, \vec{a}(\lambda)) = \frac{g_L(\vec{a}(\lambda), \vec{\alpha}) + \int_{t_{\min}}^{t_{\max}} \frac{\bar{f}(t, \vec{\alpha}, \vec{a}(\lambda))}{w(t, \vec{\alpha}, \vec{a}(\lambda))}\, \mathrm{d}t}{\int_{t_{\min}}^{t_{\max}} \frac{1}{w(t, \vec{\alpha}, \vec{a}(\lambda))}\, \mathrm{d}t}, \tag{15}$$

with

$$g_L(\vec{a}(\lambda), \vec{\alpha}) = \int_{t_{\min}}^{t_{\max}} f(\vec{a}(\lambda) + t\vec{\alpha})\, \mathrm{d}t = g(\lambda, \vec{\alpha}), \tag{16}$$

which is the cone-beam projection from $\vec{a}(\lambda)$ in the direction $\vec{\alpha}$.

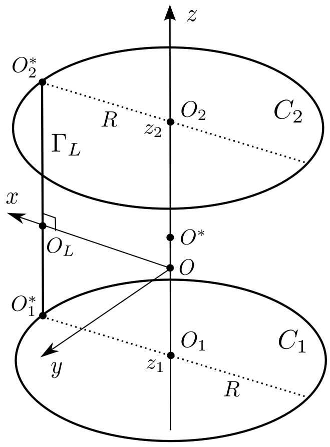

Figure 4. The coordinate system for the two-circles-plus-one-line configuration.

2.3. Reconstruction for the two-circles-plus-one-line trajectory

In this subsection, we apply the M-line reconstruction method described in the previous subsection to the two-circles-plus-one-line trajectory $\vec{a}$ in our system. This trajectory $\vec{a}$ consists of two circles C_1 and C_2 with the same radius R in two parallel planes, respectively, and one line segment Γ_L perpendicular to the two planes as shown in figure 4. The centres of the two circles are at O_1 and O_2, respectively. The midpoint between O_1 and O_2 is at O^*. The line from O_1 to O_2 is perpendicular to the two circle planes. The line segment Γ_L intersects the two circles C_1 and C_2 at $O_1^* \in C_1$ and $O_2^* \in C_2$, respectively. The two circles are oriented counterclockwise.

A coordinate system for the two-circles-plus-one-line configuration is introduced as follows. The z-axis in the coordinate system is the line from O_1 to O_2. The origin O of the coordinate system is chosen to be any point between O_1 and O_2. The orthogonal projection of the origin O on the line segment Γ_L is at O_L. The x-axis is the line from O to O_L. The y-axis is perpendicular to the xz plane such that the coordinate system xyz is right-hand oriented. In this coordinate system, the two circles C_1 and C_2 are located at the planes $z = z_1$ and $z = z_2$, respectively. The two-circles-plus-one-line trajectory $\vec{a}$ can be represented as follows:

$$\vec{a}(\lambda) = \begin{cases} (R\cos(\lambda), R\sin(\lambda),\ z_1) & \text{for } \lambda \in [0, 2\pi), \\ \left(R, 0, z_1 + \dfrac{(\lambda - 2\pi)}{2\pi}(z_2 - z_1)\right) & \text{for } \lambda \in [2\pi, 4\pi), \\ (R\cos(\lambda),\ R\sin(\lambda),\ z_2) & \text{for } \lambda \in [4\pi, 6\pi). \end{cases} \tag{17}$$

Let Σ be the region inside the two-circles-plus-one-line trajectory:

$$\Sigma = \{(x, y, z)\colon x^2 + y^2 < R^2,\ z_1 < z < z_2\}, \tag{18}$$

and Ω be the support of f which locates strictly inside Σ.

In this paper, the reconstruction of f is performed slice by slice for parallel slices perpendicular to the z-axis, as shown in figure 5. For each such slice, the M-line reconstruction method is applied to the following M-lines:

$$L(\vec{\alpha}, \vec{a}(\lambda)) :\ \lambda \in [2\pi, 4\pi),\ \vec{\alpha} \perp z\text{–axis}, \tag{19}$$

where $\vec{a}(\lambda)$ is the intersection point of the slice and line segment Γ_L. Since each slice is covered by the M-lines in equation (19), Ω can be fully covered by the M-lines. Alternatively,

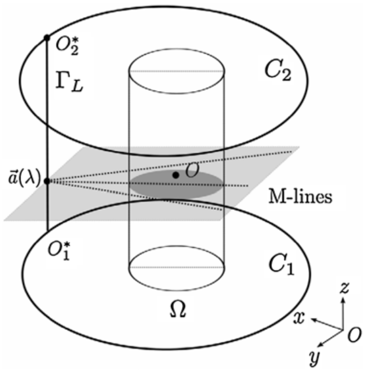

Figure 5. The reconstruction of f is performed slice by slice for parallel slices perpendicular to the z-axis. For each such slice (heavily shadowed area in the figure), M-lines $L(\vec{\alpha}, \vec{a}(\lambda))$ with $\vec{a}(\lambda) \in \Gamma_L$ and $\vec{\alpha} \perp z-$axis are chosen for reconstruction.

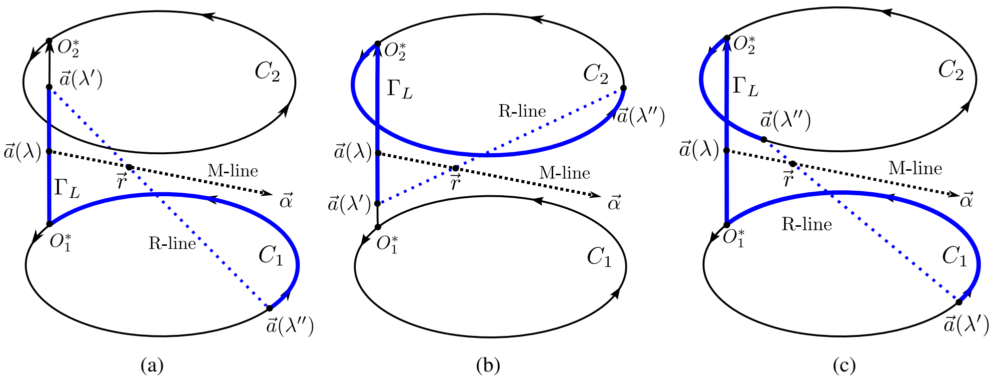

Figure 6. The backprojection intervals for $\vec{r} \in L(\vec{\alpha}, \vec{a}(\lambda))$ in the three cases (bold curves). (a) Case $\Gamma_L - C_1$. (b) Case $\Gamma_L - C_2$. (c) Case $C_1 - C_2$.

the reconstruction of f can be conducted slice by slice for parallel slices perpendicular to the x-axis or y-axis, respectively. M-lines can be chosen accordingly.

For the M-line reconstruction method, the first step is to obtain the Hilbert transform of f along one M-line $L(\vec{\alpha}, \vec{a}(\lambda))$ by equation (11). For the M-line in equation (19), there are three cases for R-lines passing though one point $\vec{r} \in L(\vec{\alpha}, \vec{a}(\lambda)) \cap \Omega$, as follows.

Case $\Gamma_L - C_1$. $\vec{r}$ is on one R-line from the line segment Γ_L to the circle C_1.
Case $\Gamma_L - C_2$. $\vec{r}$ is on one R-line from the line segment Γ_L to the circle C_2.
Case $C_1 - C_2$. $\vec{r}$ is on one R-line from the circle C_1 to the circle C_2.

The R-lines are called $\Gamma_L - C_1$ R-line, $\Gamma_L - C_2$ R-line and $C_1 - C_2$ R-line, respectively, in the following. Denote $\vec{r} = (x, y, z)$. For each case, equation (11) is specified as follows.

Case $\Gamma_L - C_1$.

If $\vec{r}$ is on one $\Gamma_L - C_1$ R-line as shown in figure 6(a), the two source positions on this R-line will be

$$\vec{a}(\lambda') = (R, 0, z_L), \qquad \vec{a}(\lambda'') = \frac{1}{1-t_1}(x, y, z) - \frac{t_1}{1-t_1}(R, 0, z_L), \tag{20}$$

for some $\lambda' \in [2\pi, 4\pi)$ and $\lambda'' \in [0, 2\pi)$ where

$$z_L = z_1 + \frac{(z - z_1)}{t_1} \qquad \text{and} \qquad t_1 = \frac{R^2 - (x^2 + y^2)}{2(R^2 - xR)}. \tag{21}$$

In this case, equation (11) becomes

$$\begin{aligned} Hf(t, \vec{\alpha}, \vec{a}(\lambda)) &= \frac{-1}{2\pi}(\bar{B}(\vec{r}, \lambda, \lambda') + \bar{B}(\vec{r}, \lambda, \lambda'')) \\ &= \frac{-1}{2\pi}(\bar{B}(\vec{r}, \lambda, \lambda') - \bar{B}(\vec{r}, \lambda'', 2\pi) - \bar{B}(\vec{r}, 2\pi, \lambda)), \end{aligned} \tag{22}$$

where $\bar{B}(\vec{r}, \lambda_1, \lambda_2)$ is given in equation (10). Then the Hilbert transform of f at $\vec{r}$ along the M-line can be computed by equation (22).

Case $\Gamma_L - C_2$.

The $\Gamma_L - C_2$ R-line can be obtained similarly to case $\Gamma_L - C_1$ according to geometric symmetry of the trajectory, as shown in figure 6(b). Equation (11) becomes

$$Hf(t, \vec{\alpha}, \vec{a}(\lambda)) = \frac{-1}{2\pi}(-\bar{B}(\vec{r}, \lambda', \lambda) + \bar{B}(\vec{r}, \lambda, 4\pi) + \bar{B}(\vec{r}, 4\pi, \lambda'')). \tag{23}$$

Case $C_1 - C_2$.

If $\vec{r}$ is on one $C_1 - C_2$ R-line as shown in figure 6(c), the two source positions on this R-line will be

$$\vec{a}(\lambda') = \frac{1}{1-t}(x - x_0, y - y_0, z - tz_2), \qquad \vec{a}(\lambda'') = \frac{1}{t}(x_0, y_0, tz_2) \tag{24}$$

for some $\lambda' \in [0, 2\pi)$ and $\lambda'' \in [4\pi, 6\pi)$ where

$$t = \frac{z - z_1}{z_2 - z_1} \tag{25}$$

and (x_0, y_0) are the real solutions of the following system of equations:

$$\begin{cases} (x - x_0)^2 + (y - y_0)^2 = (1-t)^2 R^2 \\ x_0^2 + y_0^2 = t^2 R^2. \end{cases} \tag{26}$$

Two solutions of equation (26) are

$$\begin{cases} x_0 = \dfrac{1}{r^2}\left(x\delta \pm y\sqrt{t^2 r^2 R^2 - \delta^2}\right) \\ y_0 = \dfrac{1}{r^2}\left(y\delta \mp x\sqrt{t^2 r^2 R^2 - \delta^2}\right), \end{cases} \tag{27}$$

where $r^2 = x^2 + y^2$ and $\delta = (r^2 - (1 - 2t)R^2)/2$.

Equation (11) becomes

$$\begin{aligned} Hf(t, \vec{\alpha}, \vec{a}(\lambda)) &= \frac{-1}{2\pi}(\bar{B}(\vec{r}, \lambda, \lambda') + \bar{B}(\vec{r}, \lambda, \lambda'')) \\ &= \frac{-1}{2\pi}(-\bar{B}(\vec{r}, \lambda', 2\pi) - \bar{B}(\vec{r}, 2\pi, \lambda) + \bar{B}(\vec{r}, \lambda, 4\pi) + \bar{B}(\vec{r}, 4\pi, \lambda'')). \end{aligned} \tag{28}$$

Then the Hilbert transform of f at $\vec{r}$ along the M-line can be computed by equation (28).

In Yu *et al* (2011), it has been proved that the regions covered by $\Gamma_L - C_1$, $\Gamma_L - C_2$ and $C_1 - C_2$ R-lines are the following regions Σ_1, Σ_2 and Σ_3, respectively:

$$\Sigma_1 = \{(x, y, z)\colon\ (x - tR)^2 + y^2 \leqslant (1-t)^2 R^2,\ z_1 < z < z_2\}, \tag{29}$$

$$\Sigma_2 = \{(x, y, z)\colon\ (x - (1-t)R)^2 + y^2 \leqslant t^2 R^2,\ z_1 < z < z_2\}, \tag{30}$$

$$\Sigma_3 = \{(x, y, z)\colon\ (1-2t)^2 R^2 \leqslant x^2 + y^2 < R^2, z_1 < z < z_2\}, \tag{31}$$

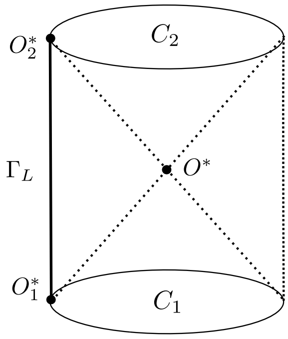

Figure 7. The geometrical descriptions of Σ, Σ_1, Σ_2 and Σ_3.

Table 1. The number of R-lines for each point in Σ except O.

Region	Number of $\Gamma_L - C_1$ and $\Gamma_L - C_2$ R-lines	Number of $C_1 - C_2$ R-lines
Σ/Σ_3	1	0
$\partial\Sigma_3 \cap \Sigma_-$	2	1
$\partial\Sigma_3 \cap (\Sigma/\Sigma_-)$	1	1
$(\Sigma_3/\partial\Sigma_3) \cap \Sigma_-$	2	2
$(\Sigma_3/\partial\Sigma_3) \cap (\Sigma_+/\Sigma_-)$	1	2
$(\Sigma_3/\partial\Sigma_3) \cap (\Sigma/\Sigma_+)$	0	2

where t is defined in equation (25). The geometrical descriptions of these regions are provided in figure 7. Σ is the cylinder with bases C_1 and C_2. Σ_1 is a cone with vertex $O_2^* \in C_2$ and base C_1, and Σ_2 is a cone with vertex $O_1^* \in C_1$ and base C_2. Σ_3 is the complementary set, with respect to Σ, of two cones with a common vertex O^* and bases C_1 and C_2. Moreover, $\Sigma = \Sigma_1 \cup \Sigma_2 \cup \Sigma_3$. Thus for each $\vec{r} \in \Omega \cap L(\vec{\alpha}, \vec{a}(\lambda))$, according to $\vec{r} \in \Sigma_d$ for some $d \in \{1, 2, 3\}$, $Hf(t, \vec{\alpha}, \vec{a}(\lambda))$ can be obtained for $t \in [t_{\min}, t_{\max}]$ by one of the equations (22), (23) and (28). Then f can be reconstructed on this M-line using the finite Hilbert transform equation (12). By M-line reconstructions on $L(\vec{\alpha}, \vec{a}(\lambda))$ for all $\vec{a}(\lambda) \in \Gamma_L$ and $\vec{\alpha} \perp z$—axis as in equation (19), f can be reconstructed all over Ω.

2.4. Analysis of R-lines

In this subsection, we investigate the number of R-lines for each point, and present how to select one proper R-line for each point. Without loss of generality, we take $z_1 = -z_2$ and $O = O^*$ in the following.

According to the geometrical descriptions, the three regions Σ_1, Σ_2 and Σ_3 do overlap with each other. Let

$$\Sigma_+ = \Sigma_1 \cup \Sigma_2, \quad \Sigma_- = \Sigma_1 \cap \Sigma_2 \tag{32}$$

and

$$\partial\Sigma_3 = \{(x, y, z)\colon x^2 + y^2 = (1 - 2t)^2 R^2, z_1 < z < z_2\}. \tag{33}$$

For the origin O, there exist one $\Gamma_L - C_1$ R-line, one $\Gamma_L - C_2$ R-line and infinite $C_1 - C_2$ R-lines. We summarize the number of R-lines for other points in table 1. We also provide the intersection of the regions in table 1 and a slice $z = z_0$ in figure 8.

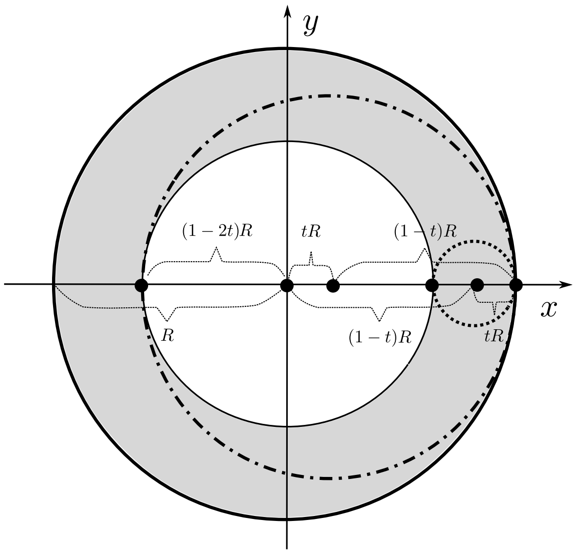

Figure 8. The intersections of Σ_i for $i = 1, 2, 3$ and one slice $z = z_0$ with $z_0 < 0$ (i.e. $t < 0.5$). The region inside the dash dotted circle represents Σ_1, and the region inside the dotted circle represents Σ_2. The annular grey region between two solid circles represents Σ_3.

From table 1, there are at least two R-lines passing through $\vec{r} \in \Sigma_3$. In the following, we introduce how to select one proper R-line for each point, such that sudden jumps can be avoided in the segment of the source trajectory used by points on each M-line in equation (19).

(a) $\vec{r} \in \Sigma/\Sigma_3$. We choose $\Gamma_L - C_1$ and $\Gamma_L - C_2$ R-lines for $z \leqslant 0$ and $z > 0$, respectively.
(b) $\vec{r} \in \Sigma_3 \cap \Sigma_+$. We choose R-lines as in (a).
(c) $\vec{r} \in \Sigma_3 \cap (\Sigma/\Sigma_+)$. For $z \leqslant 0$, we choose the $C_1 - C_2$ R-line with endpoints in equation (24) satisfying

$$\begin{cases} x_0 = \dfrac{1}{r^2}\left(x\delta + \operatorname{sgn}(y)y\sqrt{t^2r^2R^2 - \delta^2}\right) \\ y_0 = \dfrac{1}{r^2}\left(y\delta - \operatorname{sgn}(y)x\sqrt{t^2r^2R^2 - \delta^2}\right). \end{cases} \tag{34}$$

For $z > 0$, we choose the $C_1 - C_2$ R-line similarly according to the geometric symmetry of the trajectory.

We explain the method as follows. For $\vec{r} \in \Sigma/\Sigma_3$ in (a), the $\Gamma_L - C_1$ or $\Gamma_L - C_2$ R-line is the only choice. For $\vec{r} \in \Sigma_3 \cap \Sigma_+$ in (b), there are both $\Gamma_L - C_1/\Gamma_L - C_2$ and $C_1 - C_2$ R-lines. We choose the same type of R-lines as in (a) to avoid sudden jumps. For the boundary point $\vec{r} \in \partial\Sigma_+$, because the $\Gamma_L - C_1$ R-line passing through $\vec{r}$ has an endpoint $O_2^* \in \Gamma_L \cap C_2$, the $\Gamma_L - C_1$ R-line can also be considered as a $C_1 - C_2$ R-line determined by equation (34). Similar discussions can be conducted for the $\Gamma_L - C_2$ R-line. For $\vec{r} \in \Sigma_3 \cap (\Sigma/\Sigma_+)$ in (c), there are two $C_1 - C_2$ R-lines. We choose the same type of $C_1 - C_2$ R-line as $\vec{r} \in \partial\Sigma_+$. Because sgn (y) in equation (34) keeps unchanged for points on each single M-line in equation (19), the segment of the trajectory used for points in (c) has no sudden jumps.

2.5. Practical issues

In this subsection, we discuss two practical issues in our algorithm.

Table 2. Parameters for the numerical study of the Shepp–Logan phantom.

Scanning radius of the circle	3	Circle planes	$z = \pm 1$
Scanning length of the line segment	2	Detector size	221×441
Source to detector distance	3	Detector pixel size	0.01
Number of projections per circle	720	Radius of the support	1.1
Number of projections per length 1	100	Reconstruction matrix	$221 \times 221 \times 201$
Sampling interval of the M-lines	0.004	Reconstruction pixel size	0.01

The first issue is about the data usage. In the backprojection step, the direct use of equations (22), (23) and (28) will cause ineffective use of projections from both ends of the source trajectory. In the following we provide an alternative method to compute the differential backprojection which utilizes all projections on the circles for each point. By equations (9) and (10), it follows that

$$\bar{B}(\vec{r}, 0, \lambda) + \bar{B}(\vec{r}, \lambda, 2\pi) = 0, \tag{35}$$

for any $\lambda \in (0, 2\pi)$. Thus

$$\bar{B}(\vec{r}, \lambda, 2\pi) = \tfrac{1}{2}(\bar{B}(\vec{r}, \lambda, 2\pi) - \bar{B}(\vec{r}, 0, \lambda)). \tag{36}$$

Similar discussions can be conducted for $\lambda \in (4\pi, 6\pi)$.

The second issue is about the computation of derivatives in the backprojection step. In order to compute derivatives of piecewise smooth functions, following the upwind idea in computational fluid dynamics (Courant *et al* 1952), we use the one-sided finite difference scheme at the location of a jump to reduce the numerical errors. By comparing the difference between the projection values with a threshold, we select forward or backward finite difference to get the derivative value and effectively avoid using stencils across the jump.

3. Experiments

Four experiments are conducted for the proposed two-circles-plus-one-line trajectory. Three numerical studies are with the Shepp–Logan phantom, the FORBILD head phantom and a line-pair phantom. A preliminary physical phantom experiment is conducted with a wax phantom with thin aluminium wires and small aluminium fritters inside. In our implementation, the Hilbert transform in equation (14) and finite inverse Hilbert transform in equation (12) are computed with the same method as in Noo *et al* (2003), Yu and Wang (2004) and (Pack *et al* 2005), respectively. In the following, the support of f is a cylinder with the same length of Σ. The algorithm proposed in sections 2.3 and 2.4 is applied for reconstruction.

The computing environment is as follows. The computer is a DELL Precision 670 Workstation (CPU: Intel® Xeon™ 2.80 GHz; memory: 6 GB) under Linux (OPEN SUSE 11.2 x86-64). The M-line reconstruction algorithm is implemented in the **R** language, which is a popular statistical programming environment (R Development Core Team 2010). The *bigmemory* package of R supports multiple-gigabyte matrices and enables the algorithm to run successfully even when matrices involved in our implementation exceed the available RAM in the workstation (Kane and Emerson 2010).

3.1. Numerical study 1: the Shepp–Logan phantom

In this experiment, we use a 3D low contrast Shepp–Logan phantom with ten ellipsoids to test the algorithm (Kak and Slaney 1988). The parameters for the simulation are given in table 2. This reconstruction takes about 2 h. The reconstruction images of the slices at the planes

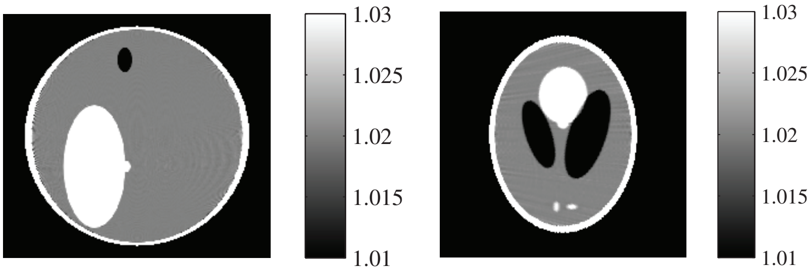

(a) (b)

Figure 9. The reconstructed images of the Shepp–Logan phantom at the planes (a) $x = 0$ and (b) $z = -0.25$. The display window is [1.01,1.03].

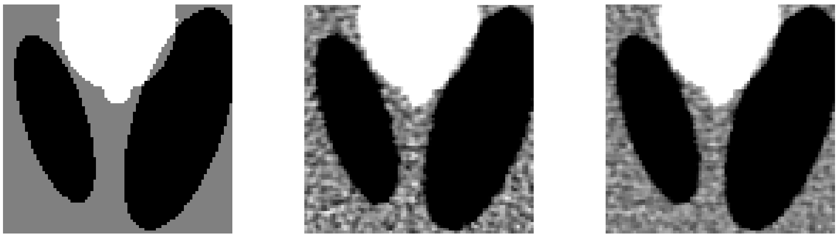

(a) (b) (c)

Figure 10. The images of the Shepp–Logan phantom at the plane $z = -0.25$ with $|x| < 0.3$, $|y| < 0.3$. (a) The original image; (b) the reconstructed image using equations (22) and (28); (c) the reconstructed image using equation (36). The display window is [1.01,1.03].

Table 3. Parameters for the numerical study of the FORBILD head phantom.

Scanning radius of the circle	30 cm	Circle planes	$z = \pm 15$ cm
Scanning length of the line segment	30 cm	Detector size	801×1401
Source to detector distance	30 cm	Detector pixel size	0.05 cm
Number of projections per circle	720	Radius of the support	14 cm
Number of projections per length 1	20	Reconstruction matrix	$601 \times 601 \times 601$
Sampling interval of the M-lines	0.04 cm	Reconstruction pixel size	0.05 cm

$x = 0$ and $z = -0.25$ are shown in figure 9. The display window is [1.01, 1.03] for images to demonstrate the low contrast structures.

Gaussian noise with standard deviation of 5 is added into 16-bit grey scale projection images with 15% saturation (set the maximum grey scale as 10 000). The reconstructed image using equations (22) and (28) is shown in figure 10(b). The reconstructed image using equation (36) is shown in figure 10(c). The total relative error of the two reconstructed images is 16.99 and 13.79, respectively. The results demonstrate that the usage of all projections on the circles can improve the performance of the algorithm for noisy data.

3.2. Numerical study 2: the FORBILD head phantom

In this experiment, we use the FORBILD head phantom without ears which contains both low and high density objects (www.imp.uni-erlangen.de/phantoms/head/head.html). The parameters for the simulation are given in table 3. This reconstruction takes about 26 h. The

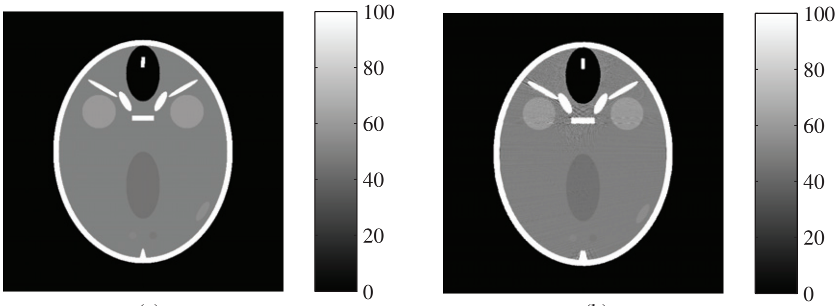

(a) (b)

Figure 11. The reconstructed images of the FORBILD head phantom at the plane $z = 0$. (a) The original image and (b) the reconstructed image. The display window is [0,100] HU.

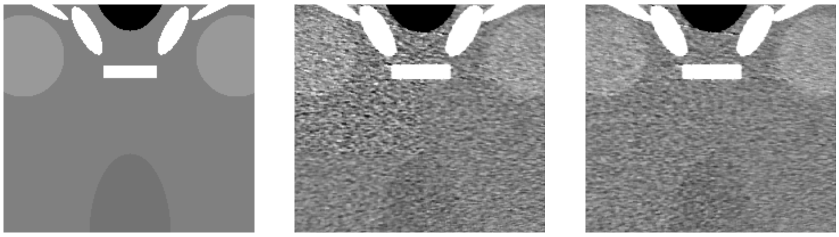

(a) (b) (c)

Figure 12. The images of the FORBILD head phantom at the plane $z = 0$ with $|x| < 5.5$, $-6.5 < y < 3.5$. (a) The original image; (b) reconstructed image using equations (22) and (28); (c) reconstructed image using equation (36). The display window is [0,100] HU.

true image and the reconstructed image of the slice at the plane $z = 0$ are shown in figure 11. The display window is set to [0, 100] HU for images. The reconstructed images show that the algorithm performs well for low contrast regions in the presence of high density objects.

Gaussian noise with standard deviation of 5 is added into 16-bit grey scale projection images with 15% saturation (set the maximum grey scale as 10 000). The reconstructed image using equations (22) and (28) is shown in figure 12(b). The reconstructed image using equation (36) is shown in figure 12(c). The total relative error of the two reconstructed images is 815.16 and 741.68, respectively. The results show that the usage of all projections on the circles can improve the performance of the algorithm for noisy data even when the phantom has high density objects inside.

3.3. Numerical study 3: a line-pair phantom

In the third experiment we design a numerical line-pair phantom with more than 1300 small cuboids to test the spatial resolution that the XCT in our system may achieve.

The line-pair phantom is designed as follows. The support of the phantom is a cuboid of 60 mm $\times$ 60 mm $\times$ 120 mm. There are six slices of small cuboids around the planes $z =$ 0 mm, $z = \pm 22$ mm, $z = \pm 38$ mm and $y = 0$ mm, in the phantom. Each slice consists of several groups of line-pairs with different widths as 0.7, 0.5, 0.3, 0.2 and 0.1 mm. Each group consists of six cuboids with the same size. The height of all small cuboids is 0.5 mm and the

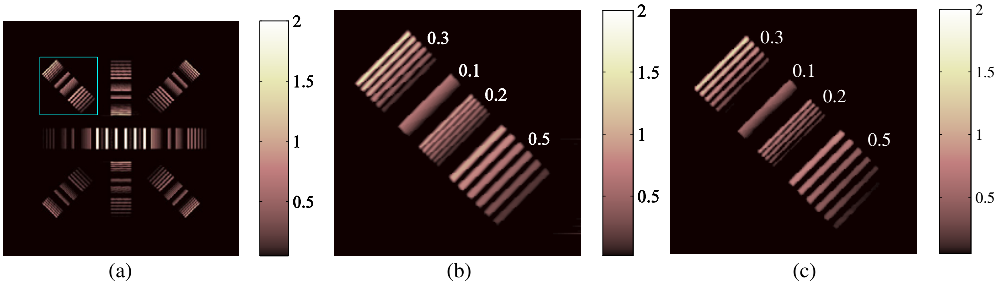

Figure 13. Pseudo-colour reconstructed images of the line-pair phantom at the plane $z = 0$ mm. (a) Reconstructed image; (b) image in the box of (a); (c) reconstructed image in the box of (a) with noise. The digital values in the images are the width of the cuboids in the line-pair groups (unit: mm). The display window is [0.05, 2].

Table 4. Parameters for the numerical simulation of the line-pair phantom.

Scanning radius of the circle	400 mm	Circle planes	$z = \pm 60$ mm
Scanning length of the line segment	120 mm	Detector size	801×1601
Source to detector distance	400 mm	Detector pixel size	0.1 mm
Number of projections per circle	360	Radius of the support	35 mm
Number of projections per length 1	2	Reconstruction matrix	$801 \times 801 \times 1201$
Sampling interval of the M-lines	0.04 mm	Reconstruction pixel size	0.1 mm

length is 3 mm. The absorption coefficient is a constant for each cuboid, but varies from 0.02 to 2 for different cuboids.

Gaussian noise with standard deviation of 30 is added into 16-bit grey scale projection images with 15% saturation (set the maximum grey scale as 10 000). The parameters for the simulation are given in table 4. The reconstruction takes about 40 h. Typical reconstructed images at the plane $z = 0$ mm are shown in figure 13. The digital values in the images are the width of the cuboids in the line-pair groups. In figures 13(b) and (c), the line-pairs whose width is 0.3 mm can be distinguished clearly while the line-pairs whose width is 0.1 mm are totally mixed. The results have demonstrated that our system can achieve a spatial resolution of 0.3 mm under this noise level, and the reconstruction of low contrast regions is sensitive to noise.

3.4. Preliminary physical phantom experiment

We have introduced rotational and translational mechanical components to the Kodak Image Station *In-Vivo* FX (Carestream Health, Inc., Rochester, NY) to enable it for XCT. After successful system calibration, we have conducted a preliminary phantom experiment with the two-circles-plus-one-line trajectory. Details of the system development and calibration will be reported in subsequent papers due to the size of the current paper.

A preliminary physical phantom is made in our lab with thin aluminium wires and small aluminium fritters (∼1 mm diameter) surrounding by wax in a cylinder container. The diameter of the region of interest (ROI) is 30.0 mm, and the length of the ROI is 60.0 mm. The one-sided finite difference scheme for computation of derivatives in section 2.5 is applied in the reconstruction.

The phantoms, its x-ray radiograph image, and the ROI are illustrated in figure 14. The parameters for the physical phantom experiment in the two-circles-plus-one-line trajectory are

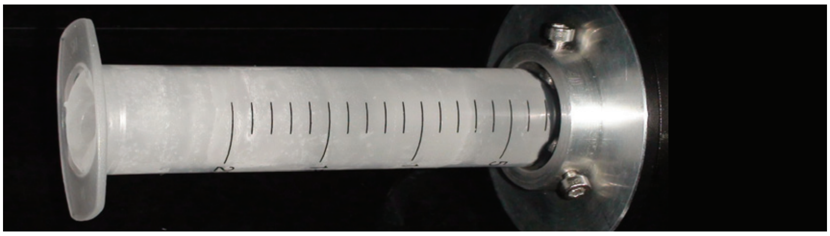

(a)

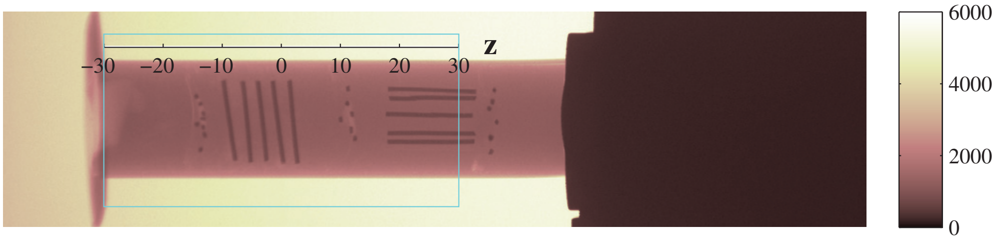

(b)

Figure 14. The phantom used for the XCT experiment and its x-ray radiograph image. (a) The phantom; (b) pseudo-colour image of the x-ray radiograph image, the ROI in the box and the length of the ROI along the z-axis. The units are mm except in the colour bars.

Table 5. Parameters for the preliminary physical phantom experiment.

Scanning radius of the circle	450.2 mm	Circle planes	$z = \pm 30$ mm
Scanning length of the line segment	60.0 mm	Detector size	401×1601
Source to detector distance	486.2 mm	Detector pixel size	0.1 mm
Number of projections per circle	360	Radius of the support	15.0 mm
Number of projections per length 1	4	Reconstruction matrix	$317 \times 317 \times 601$
Sampling interval of the M-lines	0.04 mm	Reconstruction pixel size	0.1 mm

given in table 5. The reconstructed images of a slice in the plane $z = 11.7$ mm are shown in figure 15. The reconstructed images of a slice in plane $y = 3.6$ mm are shown in figure 16. Please note that the black shade or black holes in figures 15 and 16 within the phantom image are due to blank regions in the phantom. Those blank regions contain air left in the phantom while the wax is solidifying, for which the absorption coefficients are zero.

The reconstructed images of the aluminium–wax phantom show that the 1 mm aluminium fritters can be exactly reconstructed and the absorption coefficient of the aluminium and the wax can be clearly distinguished.

4. Discussions

The x-ray module in the Kodak Image Station *In-Vivo* FX (Carestream Health, Inc., Rochester, NY) is in a cabinet with small volume. Moreover, the radiographic phosphor screen is fixed at the bottom of the left of the cabinet, which further constrains our work space to nearly half length of the cabinet. Therefore, we need to find a scanning geometry that could meet the requirement for exact cone-beam XCT reconstruction with the x-ray module.

There are several scanning geometries that can be conveniently implemented for exact cone-beam XCT reconstruction. One choice could be a scanning geometry with only circles that are not coplanar and parallel, which would require more than two rotation devices to

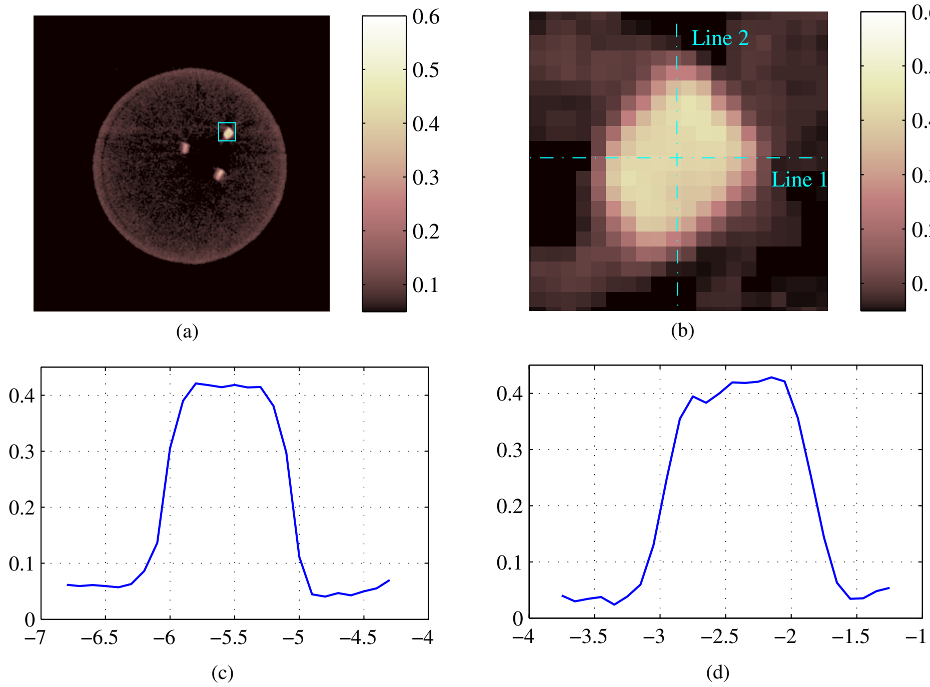

Figure 15. The reconstructed image at the plane $z = 11.7$ mm. (a) The pseudo-colour reconstructed image; (b) image in the box of (a); (c) the profile of the dash dotted line 1 in (b); (d) the profile of the dash dotted line 2 in (b). The display window is [0.05, 0.6] mm^{-1} in (a) and (b). The units of the horizontal axis and the vertical axis in (c) and (d) are mm and mm^{-1}, respectively.

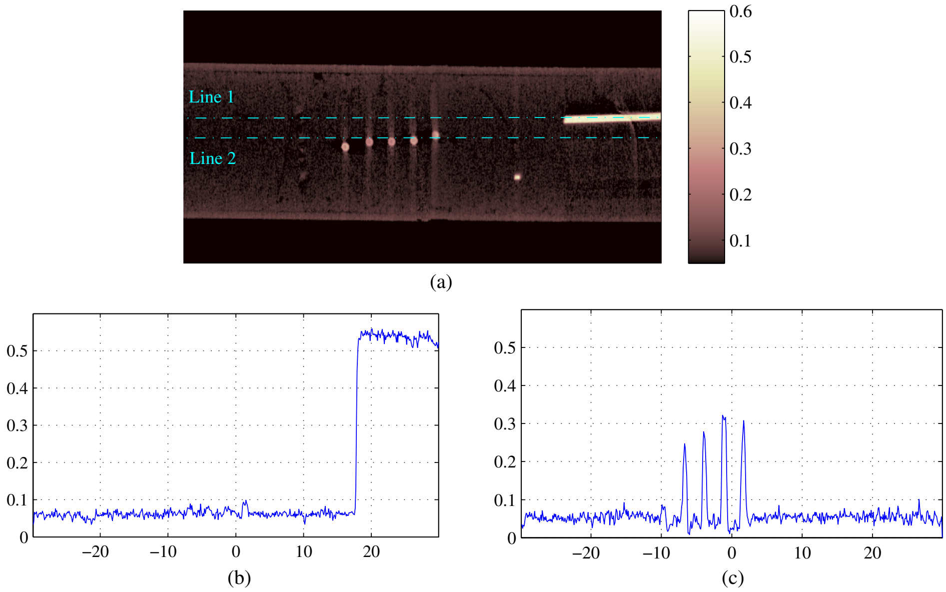

Figure 16. The reconstructed image at the plane $y = 3.6$ mm. (a) The pseudo-colour reconstructed image; (b) the profile of the dash dotted line 1 in (a); (c) the profile of the dash dotted line 2 in (a). The display window is [0.05, 0.6] mm^{-1} in (a). The units of the horizontal axis and the vertical axis in (b) and (c) are mm and mm^{-1}, respectively.

implement. Hence, we abandon this geometry with only circles because of the limited space to mount the rotation devices. Other scanning geometries are a combination of circles plus lines, and the helical trajectory. In the following, we estimate the translation length for the geometries with one circle plus one line, two circles plus one line, and the helical trajectory. We conclude that the trajectory with two circles plus one line (i.e. the two-circles-plus-one-line trajectory in previous sections) is the appropriate choice for our system.

Let the support of the object be a cylinder with radius R' and length H. Let R be the radius of circles in the geometries with one circle plus one line, two circles plus one line, and the helical trajectories, and $\mu = R'/R < 1$.

For the scanning geometry with one circle plus one line, the translation length T_1 along the line segment is estimated in Katsevich (2004a) as follows

$$T_1 = \frac{2H}{1-\mu}. \tag{37}$$

Therefore, the translation distance is twice as long as the length H of the object support.

For the scanning geometry with two circles plus one line proposed in this work, as shown in figure 4, the translation length T_2 along the line segment is equal to

$$T_2 = H. \tag{38}$$

The exact reconstruction with this geometry has been established in previous sections. Only two full rotations are required for this geometry, which is implemented with the same rotation stage in our work and does not take more space than the previous one-circle-plus-one-line trajectory and the next helical trajectory. Hence, the translation length T_2 is the same as the length H of the object support.

For the scanning geometry with the helical trajectory, the translation length T_3 should satisfy the following constraint

$$T_3 \geqslant H + \frac{1}{\pi}\,(\pi - \arccos\mu)\,(1+\mu)\,h, \tag{39}$$

where h is the helical pitch. The estimate in equation (39) could be derived from equation (33) in Yu and Wang (2004). Thus, the translation length T_3 is longer than the length H of the object support.

By comparing equations (37)–(39), the two-circles-plus-one-line trajectory takes less space than the other two geometries and hence is preferable for our system. In our implementation, we set $R = 450$ mm. For typical small animals such as mice, $H = 100$ mm, $R' = 30$ mm, we have $T_1 = 214.3$ mm, $T_2 = 100.0$ mm and $T_3 \geqslant 127.8$ mm with a pitch $h = H/2 = 50$ mm, respectively, by equations (37)–(39). We set $h = 50$ mm for the helical trajectory because the rotation in this case is about the same as in the two-circles-plus-one-line trajectory, which provides a fair basis for the comparison in both cases.

The artefacts in figure 16 are caused by under-sampling of projections for sharp, high density aluminium objects with 6–9 times absorption coefficient against the wax background. The derivatives of projection at the edges of aluminium objects are about 20 times larger than that at the wax background. Under-sampling generates errors in the backprojection step: mainly in the differential operation and integration operation as well.

As a result, the differential backprojection near aluminium objects deviates far from its true value. Then the Hilbert transform transports local backprojection errors to the whole M-line. Therefore, the reconstruction shown in figure 16 seems to exhibit strong line artefacts around aluminium objects along the direction of Hilbert transform.

In practice, we use the one-sided difference scheme with a single threshold to compute the derivatives in the physical phantom reconstruction. However, it is hard to use a single threshold to find all edges in different projection images. A method using an adaptive threshold will be developed for the one-sided difference scheme in future work.

5. Conclusion

We have proposed an improvement for the x-ray module in the Kodak Image Station by introducing a two-circles-plus-one-line trajectory for tomography. We have developed a cone-beam reconstruction algorithm by applying the M-line reconstruction method to the two-circles-plus-one-line trajectory. We have conducted numerical studies and a preliminary physical phantom experiment to demonstrate the feasibility of the proposed design and reconstruction algorithm.

Acknowledgments

This work is supported in part by the National Basic Research Program of China (973 Program) (2011CB809105), the National Science Foundation of China (61121002, 10990013, 60325101, 60872078), Key Laboratory of Machine Perception (Ministry of Education) of Peking University, and Microsoft Research of Asia. The first author would like to thank Yu Zhou for valuable discussions.

References

Alexandrakis G, Rannou F R and Chatziioannou A F 2005 Tomographic bioluminescence imaging by use of a combined optical-PET (OPET) system: a computer simulation feasibility study *Phys. Med. Biol.* **50** 4225–41

Arridge S R and Schotland J C 2009 Optical tomography: forward and inverse problems *Inverse Probl.* **25** 123010

Chen G H 2003 An alternative derivation of Katsevich's cone-beam reconstruction formula *Med. Phys.* **30** 3217–26

Courant R, Isaacson E and Rees M 1952 On the solution of nonlinear hyperbolic differential equations by finite differences *Commun. Pure Appl. Math.* **5** 243–55

Defrise M and Clack R 1994 A cone-beam reconstruction algorithm using shift-variant filtering and cone-beam backprojection *IEEE Trans. Med. Imaging* **13** 186–95

Grangeat P 1991 Mathematical framework of cone-beam 3D reconstruction via the 1st derivative of the Radon-transform in *Mathematical Methods in Tomography* (*Lecture Notes in Mathematics* vol 1497) ed G T Herman, A K Louis and F Natterer (Berline: Springer) pp 66–97

Gu X J, Zhang Q H, Larcom L and Jiang H B 2004 Three-dimensional bioluminescence tomography with model-based reconstruction *Opt. Express* **12** 3996–4000

Jiang M, Zhou T, Cheng J T, Cong W X and Wang G 2007 Image reconstruction for bioluminescence tomography from partial measurement *Opt. Express* **15** 11095–116

Kak A C and Slaney M 1988 *Principles of Computerized Tomographic Imaging* (Piscataway, NJ: IEEE)

Kane M J and Emerson J W 2010 bigmemory: manage massive matrices with shared memory and memory-mapped files (available on http://www.bigmemory.org)

Katsevich A 2002 Theoretically exact filtered backprojection-type inversion algorithm for spiral CT *SIAM J. Appl. Math.* **62** 2012–26

Katsevich A 2003 A general scheme for constructing inversion algorithms for cone beam CT *Int. J. Math. Math. Sci.* **21** 1305–21

Katsevich A 2004a Image reconstruction for the circle and line trajectory *Phys. Med. Biol.* **49** 5059–72

Katsevich A 2004b An improved exact filtered backprojection algorithm for spiral computed tomography *Adv. Appl. Math.* **32** 681–97

Kudo H and Saito T 1994 Derivation and implementation of a cone-beam reconstruction algorithm for nonplanar orbits *IEEE Trans. Med. Imaging* **13** 196–211

McLaughlin W and Vizard D 2006 Kodak *in vivo* imaging system: precise coregistration of molecular imaging with anatomical x-ray imaging in animals *Nature Methods* 26–8

Natterer F and Wübbeling F 2001 *Mathematical Methods in Image Reconstruction* (Philadelphia, PA: Society for Industrial and Applied Mathematics)

Noo F, Pack J and Heuscher D 2003 Exact helical reconstruction using native cone-beam geometries *Phys. Med. Biol.* **48** 3787–818

Ntziachristos V, Ripoll J, Wang L H V and Weissleder R 2005 Looking and listening to light: the evolution of whole-body photonic imaging *Nature Biotechnol.* **23** 313–20

Pack J D and Noo F 2005 Cone-beam reconstruction using 1D filtering along the projection of M-lines *Inverse Probl.* **21** 1105–20

Pack J D, Noo F and Clackdoyle R 2005 Cone-beam reconstruction using the backprojection of locally filtered projections *IEEE Trans. Med. Imaging* **24** 70–85

R Development Core Team 2010 R: a language and environment for statistical computing (available on http://www.R-project.org/)

Schulz R B, Ale A, Sarantopoulos A, Freyer M, Soehngen E, Zientkowska M and Ntziachristos V 2010 Hybrid system for simultaneous fluorescence and x-ray computed tomography *IEEE Trans. Med. Imaging* **29** 465–73

Smith B D 1985 Image reconstruction from cone-beam projections: necessary and sufficient conditions and reconstruction methods *IEEE Trans. Med. Imaging* **4** 14–25

Tricomi F G 1951 On the finite Hilbert transformation *Q. J. Math.* **2** 199–211

Tuy H K 1983 An inversion formula for cone-beam reconstruction *SIAM J. Appl. Math.* **43** 546–52

Wang G *et al* 2006 Recent development in bioluminescence tomography *Curr. Med. Imaging Rev.* **2** 453–7

Wang G, Li Y and Jiang M 2004 Uniqueness theorems in bioluminescence tomography *Med. Phys.* **31** 2289–99

Yalavarthy P K, Pogue B W, Dehghani H, Carpenter C M, Jiang S D and Paulsen K D 2007 Structural information within regularization matrices improves near infrared diffuse optical tomography *Opt. Express* **15** 8043–58

Ye Y B and Wang G 2005 Filtered backprojection formula for exact image reconstruction from cone-beam data along a general scanning curve *Med. Phys.* **32** 42–8

Ye Y B, Zhao S Y, Yu H Y and Wang G 2005 A general exact reconstruction for cone-beam CT via backprojection-filtration *IEEE Trans. Med. Imaging* **24** 1190–8

Yu H Y and Wang G 2004 Studies on implementation of the Katsevich algorithm for spiral cone-beam CT *J. X-Ray Sci. Technol.* **12** 97–116 (Available at http://iospress.metapress.com/content/yfmnrh9y1pemqcrp/)

Yu Z, Wunderlich A, Dennerlein F, Lauritsch G and Noo F 2011 Line plus arc source trajectories and their R-line coverage for long-object cone-beam imaging with a C-arm system *Phys. Med. Biol.* **56** 3447–71

Zhao S Y, Yu H Y and Wang G 2005 A unified framework for exact cone-beam reconstruction formulas *Med. Phys.* **32** 1712–21

Zou Y and Pan X C 2004 Exact image reconstruction on PI-lines from minimum data in helical cone-beam CT *Phys. Med. Biol.* **49** 941–59